JACS
JOURNAL OF THE AMERICAN CHEMICAL SOCIETY
pubs.acs.org/JACS
Article

Modulating Coordination Environment of Single-Atom Catalysts and Their Proximity to Photosensitive Units for Boosting MOF Photocatalysis

Xing Ma,[†] Hang Liu,[†] Weijie Yang, Guangyang Mao, Lirong Zheng, and Hai-Long Jiang*

Cite This: *J. Am. Chem. Soc.* 2021, 143, 12220−12229

ABSTRACT: Well-organized photosensitive units and catalytic sites in proximity are crucial for improving charge separation efficiency and boosting photocatalysis. Herein, a general and facile strategy for the construction of high-loading (>4 wt %) single-atom catalysts (SACs) with a tunable coordination microenvironment has been developed on the basis of metal−organic frameworks (MOFs). The neighboring $-O/OH_x$ groups from a Zr_6-oxo cluster in the MOFs provide lone-pair electrons and charge balance to immobilize the extraneous single metal atoms. The well-accessible and atomically dispersed metal sites possess close proximity to the photosensitive units (i.e., linkers), which greatly accelerates charge transfer and thereby promotes the redox reaction. The coordination environment of the representative single-atom Ni sites significantly modulates the electronic state and the proton activation barrier toward hydrogen production. As a result, the optimized Ni_1−S/MOF with a unique Ni(I) microenvironment presents excellent photocatalytic H_2 production activity, up to 270 fold of the pristine MOF and far surpassing the other Ni_1−X/MOF counterparts. This work unambiguously demonstrates the great advantage of MOFs in the fabrication of high-content SACs with variable microenvironments that are in close proximity to photosensitive linkers, thereby facilitating the electron transfer and promoting photocatalysis.

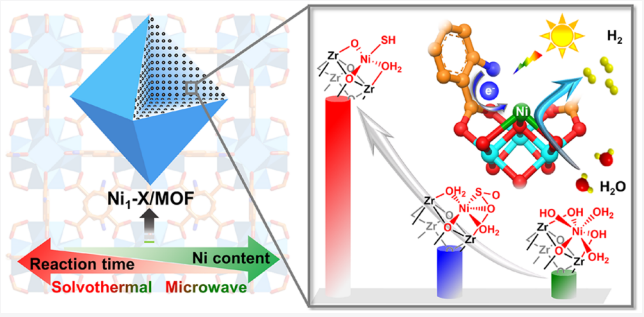

INTRODUCTION

With the rapid consumption of fossil fuels, energy shortage and environmental pollution are becoming global challenges. Solar-to-fuel conversion has attracted extraordinary interest because of the sustainability and plenty of solar energy.[1−3] Introducing effective catalytic sites (cocatalysts) to promote charge separation has been a general and proven strategy to meet the demand of efficient photocatalysis.[4−6] The photosensitive unit and catalytic sites should be in close proximity to realize this objective, facilitating the rapid electron transfer, for which their assembly in order would be preferred. Moreover, downsizing the common cocatalysts, such as metal nanoparticles (NPs), to high-loading single-atom catalysts (SACs) with good accessibility, is of great importance and benefit.[7−12] Though significant progress has been achieved, it is challenging to construct high-content SACs on traditional supports because of their limited surface.[8] To achieve stable SACs, much effort has been devoted to the construction of strong metal−support interaction to immobilize SACs and avoid undesired aggregation.[9,12−16] Unfortunately, these stabilizing strategies are unfavorable to further postmodification for central metal sites whose coordination environment modulation plays a critical role in catalysis.[17] Though there have been some investigations on the change of coordination number of SACs,[17−21] the systematic modulation of coordination environment of SACs, which might serve as a toolbox to investigate the structure−activity relationship, remains extremely rare. To meet this challenge, it is expected that suitable platforms be found that not only possess precise porous structures to stabilize SACs with high accessibility but also allow reservation of available open sites of central metal atoms for further postsynthetic modification with diverse coordination groups.

With the above considerations in mind, metal−organic frameworks (MOFs),[22−27] a class of porous crystalline solids assembled by inorganic metal ions/clusters with organic linkers, would be an ideal platform. The linkers in MOFs are able to capture photons to induce charge separation, demonstrating their feasibility and excellent role as photosensitive units in photocatalysis.[27−31] More importantly, the high porosity and structural tailorability of MOFs are very

Received: May 17, 2021
Published: July 29, 2021

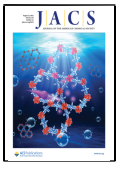

https://doi.org/10.1021/jacs.1c05032
J. Am. Chem. Soc. 2021, 143, 12220−12229

Scheme 1. Schematic Illustration Showing Ni^{2+} Decoration in UiO-66-NH_2 via an Efficient Microwave-Assisted Method and the Subsequent Coordination Environment Modulation of Single Ni Atoms to Afford Ni_1−X/MOF, in Contrast to Ni_{NP}/MOF and the One-Pot Synthesized NiS_{NP}/MOF

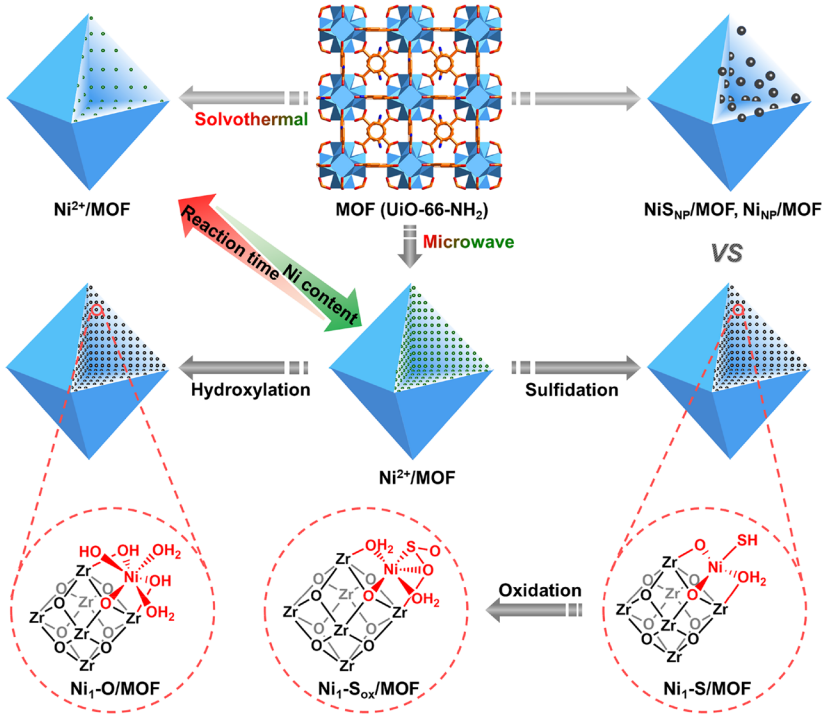

promising in the decoration of high-density metal sites, such as SACs,[22−37] which are not only able to provide suitable distance from the light-harvesting linkers but also enable coordination microenvironment modulation (MEM) with diverse functional groups.[33]

In this work, diverse Zr-based MOFs have been adopted for the facile and general construction of SACs, because the Zr_6-oxo cluster possesses neighboring surface $-O/OH_x$ sites to immobilize extraneous metal species. Specifically, a rapid and facile microwave-assisted approach is developed to furnish diverse earth-abundant metals, such as Ni^{2+}, Co^{2+}, Cu^{2+}, etc., in the single-atom form, onto the Zr_6-oxo cluster. As a representative example, the coordination environment of single-atom metals can be flexibly manipulated to afford Ni_1−X/MOF (MOF, UiO-66-NH_2 unless otherwise mentioned; Ni_1−X, Ni_1−S, Ni_1−O, Ni_1−S_{ox}; ox, oxidation) (Scheme 1). The periodic and close arrangement between light harvesting and active units in Ni_1−X/MOF significantly facilitates charge separation and the efficient electron transfer. Among these SACs, the unique sulfur-coordinated Ni(I) centers in Ni_1−S/MOF possess a reductive oxidation state and offer a much lower proton activation barrier than other counterparts. As a result, the Ni_1−S/MOF exhibits the highest activity toward photocatalytic hydrogen production under visible light irradiation, more than 270 times that of the pristine MOF and far surpassing the other Ni_1−X/MOF catalysts. To the best of our knowledge, this is the first report on boosting photocatalysis by constructing SACs with modulated microenvironment and close proximity to photosensitive linkers in MOFs.

RESULTS AND DISCUSSION

The single-atom Ni^{2+} modified UiO-66-NH_2, denoted Ni^{2+}/MOF, was obtained by the facile microwave-assisted treatment of the dispersed mixture of UiO-66-NH_2 and $NiCl_2{\cdot}6H_2O$ in CH_3CN. Upon thoroughly washing to remove excess reactants, the cyan powder of Ni^{2+}/MOF can be clearly distinguished from the parent yellowish UiO-66-NH_2 (Figure S1). Powder X-ray diffraction (XRD) patterns indicate that this modification is moderate and does not affect the MOF crystallinity (Figure S2). In contrast, such color change cannot be observed by the common impregnation method (Figure S1). Moreover, although the Ni^{2+}/MOF can also be obtained by solvothermal synthesis with much longer time, the Ni loading amounts (1.01 and 1.37 wt %) are much lower than that by microwave-assisted method (4.83 wt %) (Figure S3), based on inductively coupled plasma atomic emission spectroscopy (ICP-AES) data (Table S1). Remarkably, this microwave-assisted synthetic method was demonstrated to be powerful, general, and extendable to the MOF modification with different external metal ions (Co^{2+}, Cu^{2+}, Ru^{3+}), accompanied by significant color change (Figure S4a). In addition, such modification approach can even be extended to other MOFs with Zr_6-oxo clusters in different symmetries, such as UiO-66 in O_h symmetry, DUT-67 in D_{4h} symmetry, and MOF-808 in D_{3d} symmetry, further supporting the strong universality of this approach, which is not limited to amine-functionalized MOFs (Figure S4b−d). Powder X-ray diffraction (PXRD) patterns demonstrate the well-retained crystallinity of all these MOFs after the modification (Figure S5).

X-ray photoelectron spectroscopy (XPS) spectrum of Ni^{2+}/MOF presents the binding energy of Ni $2p_{3/2}$ at 856.3 eV (Figure S6), the typical Ni^{2+} signal, indicating that no redox process occurs during the microwave modification. The positive correlation between Ni loading content and the defect degree of the MOF suggest that the anchoring sites of Ni^{2+} ions should be dominated by $-O/OH_x$ groups on the defect sites of Zr_6-oxo cluster (Figures S7 and S8 and Table S1).[35]

https://doi.org/10.1021/jacs.1c05032
J. Am. Chem. Soc. 2021, 143, 12220−12229

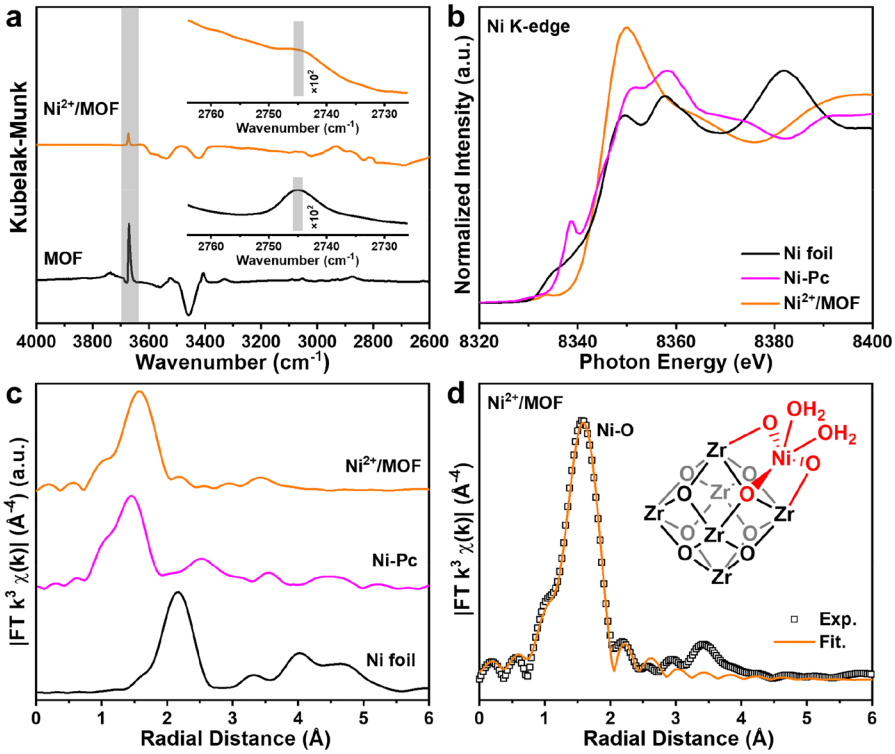

Figure 1. (a) DRIFTS spectra of Ni^{2+}/MOF and MOF (inset: enlarged spectra with the highlighted peak at 2745 cm^{-1}). (b, c) Ni K-edge XANES and FT-EXAFS spectra of Ni^{2+}/MOF, Ni foil, and Ni-Pc. (d) EXAFS fitting of Ni^{2+}/MOF (inset: proposed structure of Ni^{2+}-modified Zr_6-oxo cluster).

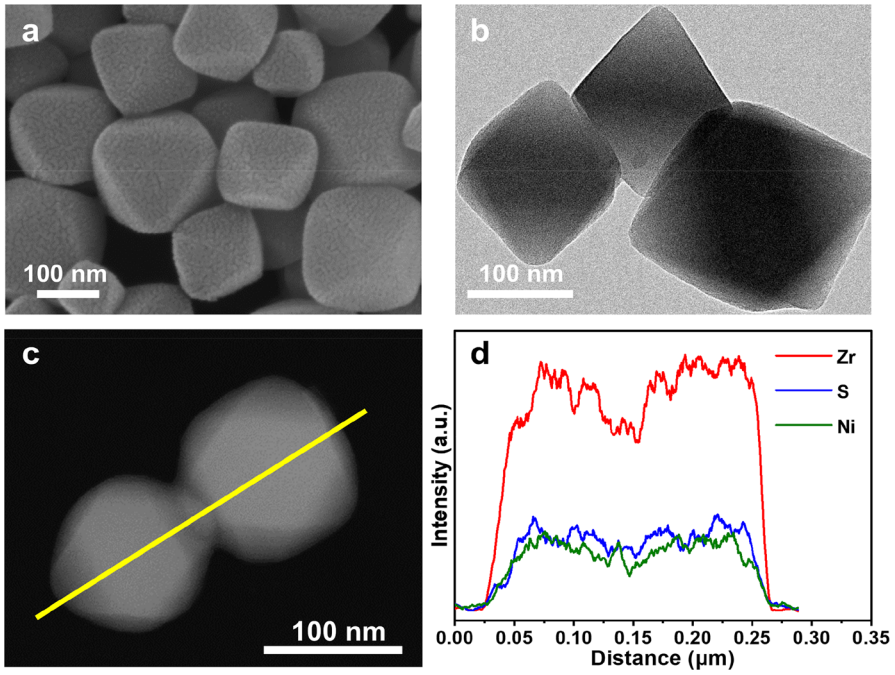

Figure 2. (a) SEM and (b) TEM images of Ni_1−S/MOF. (c, d) HAADF-STEM image and the corresponding EDS line scan profile through the particles along with the yellow line of Ni_1−S/MOF.

The bonding between Ni^{2+} and −O/OH_x groups is verified by diffuse reflectance infrared Fourier transform spectroscopy (DRIFTS). The peaks at 3670 and 2745 cm^{-1} are assignable to the terminal −OH/−OH_2 and μ_3−OH groups on the Zr_6-oxo cluster, where the peak intensity displays apparent decrease after Ni^{2+} modification, revealing the interaction of these groups with Ni^{2+} ions (Figure 1a).[38,39] To gain more information, we resorted to X-ray absorption spectroscopy (XAS) to get in-depth insight into the electronic structure and geometric structure of Ni sites. The X-ray absorption near edge spectroscopy (XANES) spectrum and differential curve of Ni^{2+}/MOF show very close absorption edge to Ni(II)-

https://doi.org/10.1021/jacs.1c05032
J. Am. Chem. Soc. 2021, 143, 12220−12229

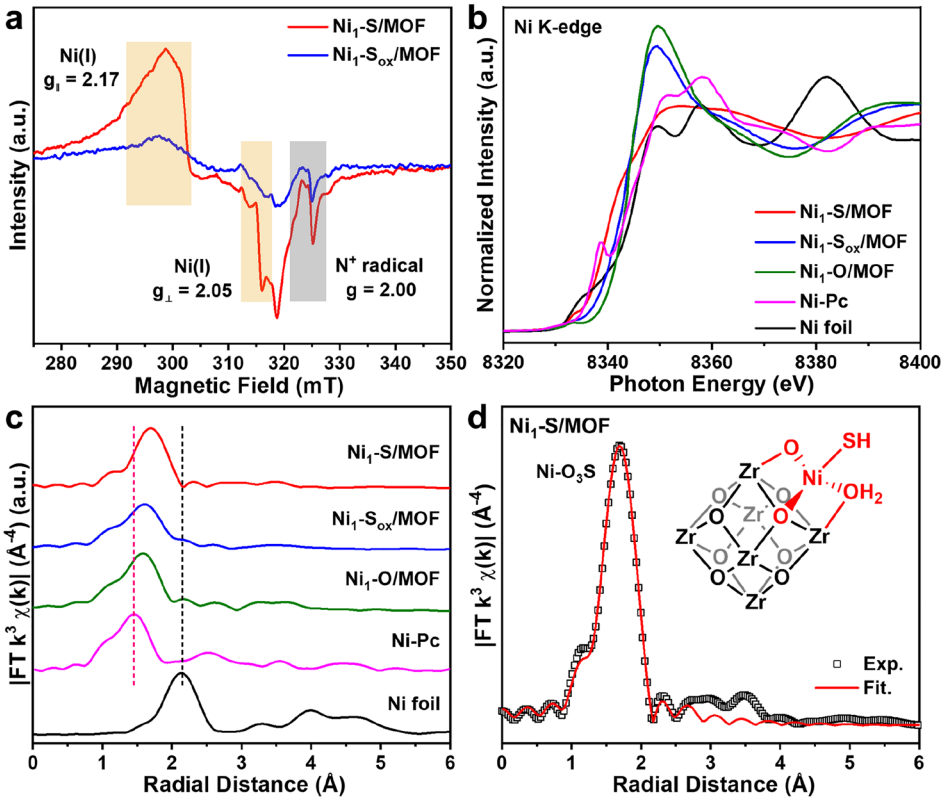

Figure 3. (a) EPR spectra of Ni_1−S/MOF and Ni_1−S_{ox}/MOF under a N_2 atmosphere. (b, c) Ni K-edge XANES and FT-EXAFS spectra of Ni_1−X/MOF, Ni foil, and Ni-Pc. (d) EXAFS fitting of Ni_1−S/MOF (inset: proposed structure of the Zr_6-oxo cluster modified by a S-coordinated Ni_1 site).

phthalocyanine (Ni-Pc) (Figure 1b and Figure S9), proving the presence of Ni^{2+}.[40] Fourier transform-extended X-ray absorption fine structure (FT-EXAFS) spectrum presents a dominated peak at ∼1.56 Å ascribed to Ni−O scattering path and no peak related to Ni−Ni bond (Figure 1c), indicating the singly dispersed Ni^{2+} sites. The curve fitting for EXAFS data further indicates the coordination environment of Ni^{2+} sites (Figure 1d, Table S2). The best fitting result for the first shell manifests that the Ni^{2+} site is five-coordinated by oxygen atoms of $-O/OH_x$ groups from Zr_6-oxo cluster and H_2O molecules, consistent with the DRIFTS results.

Given the $-O/OH_x$ groups from the Zr_6−O cluster are gathered on the one side of the Ni_1 site, its further coordination environment modulation on the other side would be feasible by postsynthetic modification. To achieve the coordination environment modulation, we have adopted thioacetamide and ammonia to react with Ni^{2+}/MOF for sulfidation and hydroxylation, respectively, affording Ni_1−S/MOF and Ni_1−O/MOF. The Ni_1−S_{ox}/MOF can be synthesized by further partial oxidation of Ni_1−S/MOF. The crystallinity and framework structure of Ni_1−X/MOF are well maintained after the above functionalized modifications (Figures S2, S10, and S11). Nitrogen sorption at 77 K indicates that all Ni_1−X/MOF remain highly porous and their BET surface areas fall into 737−885 m^2/g (Figure S12). The molar ratios of Ni and S in Ni_1−S/MOF and Ni_1−S_{ox}/MOF are all ∼1:1 (Table S1), as evaluated by the ICP-AES data.

Scanning electron microscopy (SEM) and transmission electron microscopy (TEM) images indicate that no evident particle can be observed on the surface or in the interior of the Ni_1−X/MOF (Figure 2a, b and Figure S13). The energy-dispersive X-ray spectroscopy (EDS) line scan profile indicates that the Ni and S species synchronously exist and are uniformly distributed throughout the MOF particle in Ni_1−S/MOF (Figure 2c, d). By sharp contrast, from the SEM and high-resolution transmission electron microscope (HRTEM) observations, NiS nanoparticles can be identified on the sample surface of NiS_{NP}/MOF (NP: nanoparticle) that was synthesized by the one-pot solvothermal method (Figures S1, S14, and S15). Such a striking comparison highlights the superiority of this microwave-assisted approach in the construction of atomically dispersed metal sites in MOFs. For better comparison, the Ni^{2+}/MOF was directly reduced by $NaBH_4$ to afford Ni_{NP}/MOF with good crystallinity and morphology (Figures S16 and S17a); the obvious color change from cyan to black indicates the successful reduction (Figure S1), which is further verified by the observed Ni NPs in TEM image (Figure S17b) and the uniform distribution of Ni species throughout the MOF particle by the EDS line scan profile (Figure S17c, d).

The electronic state of Ni_1−S/MOF has been investigated by XPS analysis. Interestingly, the binding energy of Ni $2p_{3/2}$ at 853.9 eV is apparently lower than that of the typical Ni^{2+} (856.5 eV) (Figure S18a), indicating the lower oxidation state of Ni site and the possible formation of Ni−S bond.[41,42] The binding energies of S 2p are at 162.7 and 169.2 eV, respectively, representing S^{2-} and S^{6+} (Figure S18b).[41] The low proportion of Ni^{2+} and S^{6+} may be due to the unavoidable partial oxidation of Ni_1−S in the run-up to the XPS test. The X-ray absorption near-edge structure (XANES) spectrum of the S K-edge further confirms the formation of Ni−S bond in Ni_1−S/MOF (Figure S19).[43,44] The reduced oxidation state of Ni sites in Ni_1−S/MOF is further supported by electron paramagnetic resonance (EPR) results, in which the $g_{\|}$ = 2.17

https://doi.org/10.1021/jacs.1c05032
J. Am. Chem. Soc. 2021, 143, 12220−12229

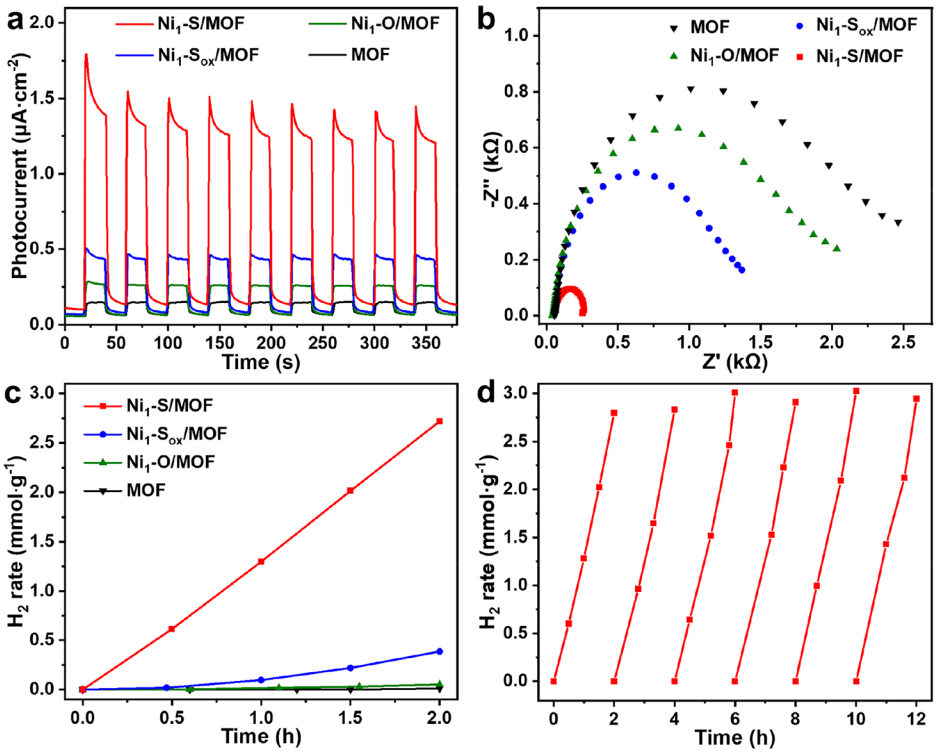

Figure 4. (a) Photocurrent responses, (b) EIS plots, (c) photocatalytic H_2 evolution rate of Ni_1−X/MOF and MOF. (d) Photocatalytic H_2 production recycling performance of Ni_1−S/MOF.

and $g_\perp$ = 2.05 signals can be assigned to Ni(I) with unpaired electron (Figure 3a).[45,46] Upon oxidation treatment to get Ni_1−S_{ox}/MOF, the Ni $2p_{3/2}$ peak at ∼853.2 eV related to the Ni(I) signal in the XPS spectrum of Ni_1−S_{ox}/MOF shows an apparent decrease (Figure S20), in line with its much weakened Ni(I) EPR signals (Figure 3a). The hydroxylated sample, Ni_1−O/MOF, featuring a Ni $2p_{3/2}$ XPS peak at 856.1 eV only, can be ascribed to the formation of Ni(II)-O bonds (Figure S21).

To gain detailed structural information for Ni_1−X/MOF, we have further studied XANES and FT-EXAFS spectra. As identified by XANES and their differential curves, the Ni_1−S/MOF shows an apparently lower absorption edge than Ni_1−S_{ox}/MOF and Ni_1−O/MOF, all locating between Ni foil and Ni-Pc, further illustrating the existence of a Ni(I) site with a reduced oxidation state by coordinating with more electron-donating groups in Ni_1−S/MOF (Figure 3b and Figure S22).[40] All FT-EXAFS spectra of Ni_1−X/MOF give one dominant peak only that presents no overlap with the Ni−Ni bond at 2.14 Å, proving the single Ni atoms are maintained during the modification (Figure 3c). By comparison of the dominant peaks for the Ni_1−X/MOF samples, Ni_1−S/MOF possesses the maximum radial distance at 1.69 Å, followed by 1.61 Å for Ni_1−S_{ox}/MOF, whereas it is 1.58 Å for Ni_1−O/MOF, which is in good agreement with the order of the coordinated S, mixed S/O, and O atom radii. Specifically, the coordination environment of the Ni_1 in all Ni_1−X/MOF samples can be obtained by the best fitting of EXAFS data (Figure 3d, Figure S23, and Table S2), verifying the successful modulation of the coordination microenvironment. Moreover, in the DRIFT spectra of Ni_1−X/MOF, the reduced peaks of terminal −OH/−OH_2 and μ_3−OH at 3672 and 2745 cm^{-1} further prove that the Ni_1−X sites are anchored onto the Zr_6-oxo cluster and inherit the bonding feature of Ni^{2+}/MOF (Figure S24).

To unveil how the different Ni dispersity and modulated microenvironment around Ni_1 sites in the MOF affect the charge separation efficiency, we have resorted to diverse photo/electrochemical techniques. UV−vis spectra show that the modification with Ni_1−X, NiS_{NP}, or Ni_{NP} does not apparently influence the light absorption ability of the MOF (or the linker), featuring the UV−vis peak at ∼370 nm (Figure S25). Compared with NiS- or Ni NP-decorated MOFs, the Ni_1−S/MOF exhibits an enhanced photocurrent response under visible irradiation, and the electrochemical impedance spectroscopy (EIS) plots show that Ni_1−S/MOF exhibits a small radius, referring reduced charge-transfer resistance (Figure S26). In line with this, the Ni_1−S/MOF exhibits significantly improved conductivity compared to that of the parent MOF and NiS_{NP}/MOF (Figure S27). Further support can be obtained by their photoluminescence emission spectra, where the characteristic peak of the MOF was significantly suppressed by incorporating Ni_1−S, indicating a rapid charge transfer process occurred (Figure S28). These results collectively highlight the advantage of constructing atomically dispersed Ni_1−S sites with close proximity to the organic linker (as photosensitizing unit). Given the stronger electron-donating microenvironment surrounding Ni_1 sites in Ni_1−S/MOF than the other counterparts such as Ni_1−O/MOF and Ni_1−S_{ox}/MOF, the former presents the highest photocurrent response and the most rapid charge transfer efficiency (Figure 4a, b and Figure S29). These observations unambiguously demonstrate that the radiative electron−hole recombination can be effectively suppressed by extracting the electrons by single-atom Ni sites with an optimized coordination environment. The distinctly different photoelectrochemical properties

https://doi.org/10.1021/jacs.1c05032
J. Am. Chem. Soc. 2021, 143, 12220−12229

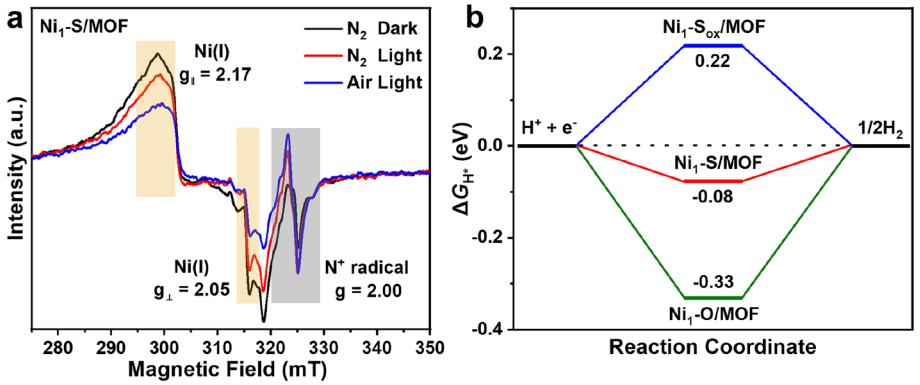

Figure 5. (a) EPR spectra of Ni_1−S/MOF under different conditions. (b) Calculated free energy diagram for photocatalytic H_2 production over Ni_1−X/MOF.

suggest that, among the investigated samples, the Ni_1−S/MOF might possess the best activity in photocatalysis.

Encouraged by the above results, we set out to investigate their photocatalytic performance for H_2 production by water splitting under visible -light irradiation in DMF with TEA as a sacrificial agent and a suitable amount of photocatalyst (Figures S30−S32). With prolonged irradiation time, the generated hydrogen amount gradually increases, proving that this is indeed a photocatalytic process (Figure 4c and Figure S33). Notably, the Ni_1−S/MOF exhibits a prominent H_2 production rate of 1360 μmol g^{-1} h^{-1}, which represents one of the highest reported visible-light activities over all reported MOF-based photocatalysts with non-noble metal cocatalyst (Table S3), not only exceeding that of NiS_{NP}/MOF (496 μmol g^{-1} h^{-1}), Ni_{NP}/MOF (128 μmol g^{-1} h^{-1}) and the MOF (5 μmol g^{-1} h^{-1}) (Figure S33), but also far surpassing that of Ni_1−S_{ox}/MOF (193 μmol g^{-1} h^{-1}) and Ni_1−O/MOF (26 μmol g^{-1} h^{-1}) (Figure 4c and Figure S34). Moreover, the introduction of suitable photosensitizer is able to further improve the activity of Ni_1−S/MOF (Figures S35 and S36). In addition, the good activity of Ni_1−S/MOF can be well-maintained for at least six cycles with intact crystallinity (Figure 4d and Figure S2), which manifests its good stability and recyclability.

To gain more insight into the excellent activity of Ni_1−S/MOF, we collected EPR spectra under the simulated reaction atmosphere for tracking catalytic process. Besides the Ni(I) signal, the peak of g = 2.00 can be ascribed to the N^+-centered radical, originating from partial oxidation of amine in the MOF (Figure 5a and Figure S37a).[47,48] For Ni_1−S/MOF, upon illumination in a N_2 atmosphere, the Ni(I) signals decrease along with an increase in the N^+-centered radical (Figure 5a), which can be attributed to charge transfer from the amine-based linker to the Ni_1 site. When the atmosphere is switched from N_2 to air, behaving as an electron acceptor to promote charge transfer, such a signal is apparently enhanced. The accordingly decreased Ni(I) signals might be ascribed to the formation of Ni(0). However, in the EPR spectra of Ni_1−S_{ox}/MOF, the Ni(I) signals are very weak with negligible signal change, whereas the signal change of the N^+ central radical can be observed (Figure S37b). The significant difference of EPR signal variations between Ni_1−S/MOF and Ni_1−S_{ox}/MOF accounts for kinetic advantage of Ni(I) site for accepting electrons, giving rise to accelerated proton reduction and much enhanced photoactivity of Ni_1−S/MOF. Accordingly, the mechanism of photocatalytic H_2 production over Ni_1−S/MOF can be proposed on the basis of the above results (Figure S38).

Furthermore, the modulation by coordination environment of single Ni atoms for hydrogen production has been evaluated by density functional theory (DFT) calculations. The models are constructed based on the periodic structure of MOF with certain modifications, and energetically optimized for DFT calculations (Figure S39). The ΔG_{H^*} (Gibbs free energy variation) of Ni_1−S/MOF is calculated to be −0.08 eV, suggesting the most efficient proton/electron transfer to form H* and its faster molecular hydrogen release than Ni_1−S_{ox}/MOF with ΔG_{H^*} of 0.22 eV, and Ni_1−O/MOF with ΔG_{H^*} of −0.33 eV (Figure 5b). The order of the energy barriers for proton activation matches well with the photocatalytic activity trend, which evidently manifests the significance of coordination environment modulation for SACs. In fact, such a sulfidation method/process to afford the optimized Ni_1−S/MOF is general and moderate, which has been demonstrated to be extendable to the successful synthesis of M_1-S/MOF (M, Co^{2+}, Cu^{2+}; MOF, UiO-66-NH_2) (Figures S40−S43), highlighting the generality of this synthetic approach.

CONCLUSIONS

In conclusion, we have developed a facile, straightforward, and general microwave-assisted method to bind diverse metal ions (Ni^{2+}, Co^{2+}, Cu^{2+}, Ru^{3+}) to Zr_6-oxo clusters in different MOFs, followed by hydroxylation, sulfidation, or further oxidation, affording MOF supported SACs with a tunable coordination environment. Among them, as a representative, a series of high-loading (>4 wt %) SACs, Ni_1−X/MOF (MOF = UiO-66-NH_2), featuring a modulated microenvironment around the Ni_1 sites on Zr_6-oxo clusters, has been fabricated for photocatalytic H_2 production. The obtained single-atom Ni_1 catalyst, presenting the highest atomic availability and close proximity to the linkers (photosensitive unit) that is favorable to charge transfer, far superior to that of corresponding NiS or Ni NPs supported by the MOF. Strikingly, among the Ni_1−X/MOF photocatalysts with different coordination microenvironments of Ni_1, the Ni_1−S/MOF involving sulfur-coordinated Ni(I) sites possesses the best charge separation efficiency and the lowest proton activation barrier. As a result, Ni_1−S/MOF exhibits excellent photocatalytic hydrogen production performance under visible light, surpassing all other counterparts. This work highlights the significance of establishing proximity between photosensitive units and catalytic sites and the

https://doi.org/10.1021/jacs.1c05032
J. Am. Chem. Soc. 2021, 143, 12220−12229

coordination microenvironment modulation of SACs in photocatalysis.

MATERIALS AND METHODS

Materials and Equipment. All chemicals were obtained from commercial sources and were used without further purification. Deionized water was obtained by reversed osmosis (the specific resistance of 18.25 MΩ·cm), followed by ion-exchange and filtration (Cleaned Water Treatment Co., Ltd., Hefei). Powder X-ray diffraction (XRD) patterns were obtained on a Japan Rigaku MiniFlex 600 equipped with graphite-monochromated Cu Kα radiation (λ = 1.54178 Å). UV−vis diffuse reflectance data were recorded on a Shimadzu UV-2700 spectrophotometer and a white standard of $BaSO_4$ was used as a reference. Gas sorption measurements were conducted by using an automatic volumetric adsorption equipment (Micromeritics ASAP 2020). Dissolution/^{1}H NMR spectra were collected on a Bruker AC-400FT spectrometer (400 MHz) with 2 M NaOH in D_2O using as digestion medium to dissolve MOFs. Transmission electron microscopy (TEM) images and scanning transmission electron microscopy-energy dispersive spectroscopy (STEM-EDS) line scan were acquired on a JEOL JEM-2100F field-emission transmission electron microscope. Catalytic H_2 generation products were analyzed and identified by gas chromatography (Shimadzu GC-2014). The contents of Ni and S in the nanocomposites were quantified by Optima 7300 DV inductively coupled plasma atomic emission spectrometer (ICP-AES) and Thermo Scientific iCAP 7400 inductively coupled plasma optic emission spectrometer (ICP-OES). Diffuse reflectance infrared spectra (DRIFTS) were recorded on a Thermo Scientific Nicolet iS10 FTIR spectrometer equipped with an MCT detector in the 4000 to 400 cm^{-1} range. Field-emission scanning electron microscopy (FE-SEM) was carried out with a field-emission scanning electron microanalyzer (Zeiss Supra 40 scanning electron microscope at an acceleration voltage of 5 kV). The X-ray photoelectron spectroscopy (XPS) measurements were performed by using an ESCALAB 250 high-performance electron spectrometer using monochromatized Al Kα ($h\nu$ = 1486.7 eV) as the excitation source.

Synthesis of UiO-66-NH_2. The synthesis is based on the previous report with modifications.[49] Generally, 186 mg (0.8 mmol) of $ZrCl_4$ and 145 mg (0.8 mmol) of H_2ATA were dissolved in 50 mL of DMF containing 6 mL of HOAc. After adding 0.5 mL of H_2O, the mixture was transferred into a 100 mL glass flask. The flask was kept at 120 °C for 12 h under continuous stirring. After being cooled to room temperature, the solid was isolated by centrifuging, and washed with DMF and acetone. The as-synthesized UiO-66-NH_2 was immersed in the acetone to exchange DMF, followed by drying at 60 °C under a vacuum. For comparison, UiO-66-NH_2-LD (LD means low defect) was synthesized by decreasing the HOAc from 6 to 0.6 mL,[50,51] whereas other parameters remain the same.

Synthesis of UiO-66-NH_2−Ideal. The synthesis is based on the previous report with modifications.[50] Generally, 378 mg (1.6 mmol) of $ZrCl_4$ and 579 mg (3.2 mmol) of H_2ATA were dissolved in 9.7 mL of DMF containing 0.29 mL of HCl (35%). The mixture was transferred into a 20 mL Teflon lined autoclave and heated in a 220 °C oven for 24 h. After being cooled to room temperature, the solid was isolated by centrifuging and washed with DMF and acetone. The as-synthesized UiO-66-NH_2−Ideal was immersed in the acetone to exchange DMF, followed by drying at 60 °C under a vacuum prior to use.

Synthesis of RhB@UiO-66-NH_2. RhB@UiO-66-NH_2 was obtained by a similar synthetic process as for UiO-66-NH_2, except for adding an additional 30 mg of RhB as a reactant.

Synthesis of EY@UiO-66-NH_2. EY@UiO-66-NH_2 was obtained by a similar synthetic process as for UiO-66-NH_2, except for adding an additional 30 mg of EY as a reactant.

Synthesis of UiO-66. UiO-66 was obtained by similar synthesis conditions as for UiO-66-NH_2, except for replacing the H_2ATA with the same molar amount of H_2BDC, 138 mg (0.8 mmol), and changing the added water amount to 0.1 mL.

Synthesis of MOF-808. The MOF-808 was synthesized according to the previous report with some modifications.[52] Typically, 97 mg (0.54 mmol) of $ZrOCl_2·8H_2O$, 21 mg (0.1 mmol) of H_3BTC, and 3 mL of formic acid in 3 mL of DMF were ultrasonically dissolved in a 20 mL Teflon-lined autoclave and heated in a 100 °C oven for 24 h. The solid was separated by centrifuging and washed with DMF and acetone. The as-synthesized MOF-808 was immersed in acetone and dried at 60 °C under a vacuum.

Synthesis of DUT-67. The DUT-67 was synthesized according to the previous literature with some modification.[53] Typically, 229 mg (1.28 mmol) of $ZrOCl_2·8H_2O$, 644 mg (3.74 mmol) of H_2TDC were dispersed ultrasonically in 10 mL of DMF and 10 mL of HOAc. The mixture was transfer into a 35 mL microwave vessel and sealed. The reaction was then rapidly heated to 95 °C by CEM Discover and held at this temperature for 1 h with continuously stirring. After being cooled to room temperature, the solid was isolated by centrifuging and washed with 0.1 M NaOAc aqueous solution and water. The as-synthesized DUT-67 was immersed in acetone to exchange the H_2O, followed by drying at 60 °C under a vacuum.

Microwave-Assisted Synthesis of Ni^{2+}/MOF. Generally, 40 mg of UiO-66-NH_2 and 200 mg of $NiCl_2·6H_2O$ were added into a 10 mL microwave vessel, followed by adding 6 mL of MeCN. The mixture was then rapidly heated to 85 °C by CEM Discover and held at this temperature for 30 min with continuous stirring. After being cooled to room temperature, the solid was isolated by centrifuging, washed with DMF and MeCN, and finally dried at 60 °C under a vacuum to afford Ni^{2+}/MOF (microwave). Proton solvent should be avoided during this process, as it will lead to the detachment of Ni^{2+} ions. RhB@Ni^{2+}/MOF and EY@Ni^{2+}/MOF were obtained by a similar synthetic process as for Ni^{2+}/MOF, except for replacing the MOF with the same amount of RhB@MOF and EY@MOF, respectively. By comparison, the other two Ni^{2+}-modified samples as controls were also prepared by solvothermal synthesis. For the synthesis of Ni^{2+}/MOF (solvothermal, MeCN), 20 mg of UiO-66-NH_2, 100 mg of $NiCl_2·6H_2O$, and 3 mL of MeCN were mixed in the glass vial and heated at 85 °C with continuous stirring for 24 h. For the synthesis of Ni^{2+}/MOF (solvothermal, DMF), 20 mg of UiO-66-NH_2, 100 mg of $NiCl_2·6H_2O$, and 3 mL of DMF were mixed in the glass vial and heated at 85 °C with continuous stirring for 2 h. These two samples were fully washed by DMF and MeCN prior to the ICP-AES tests.

Synthesis of Other Cation-Modified MOFs. The other MOFs with Zr_6-oxo clusters in different symmetries, such as MOF-808 and DUT-67, can also be adopted for the metal cation modification. Notably, the metal salts must be chloride salts and the involved water seems not necessary, such as $RuCl_3$, $CoCl_2·6H_2O$, $CuCl_2·2H_2O$, etc. Nevertheless, it is found that the less water content there is in the system, the more stable the modified cations will be in the resulting MOFs. The other reaction conditions are kept the same as the above-mentioned microwave synthesis for Ni^{2+}/MOF (microwave).

Synthesis of Ni_1−S/MOF. Generally, 20 mg of Ni^{2+}/MOF was dispersed in 2 mL of DMF, followed by adding 50 mg of thioacetamide (TAA). The mixture was sealed into a custom-designed glass reaction tube. The tube was frozen by liquid nitrogen, air was pumped out, and the tube was backfilled with protective gas with a N_2 balloon. The reaction tube was heated at the temperature of 120 °C under stirring for 1 h. The resulting black solid was washed with DMF and acetone, then dried under a vacuum at room temperature. RhB@Ni_1−S/MOF and EY@Ni_1−S/MOF were obtained by a similar synthetic process as for Ni_1−S/MOF, except for replacing the Ni^{2+}/MOF with the same amount of RhB@Ni^{2+}/MOF and EY@Ni^{2+}/MOF, respectively.

Synthesis of Ni_1−S_{ox}/MOF. To synthesize Ni_1−S_{ox}/MOF, we partially oxidized 20 mg of Ni_1−S/MOF under an air atmosphere in an oven at 85 °C for 1 day.

Synthesis of Ni_1−O/MOF. Generally, 20 mg of Ni^{2+}/MOF was dispersed in 2 mL of DMF, followed by adding 2 mL of $NH_3·H_2O$. The mixture was then rapidly heated to 60 °C by a CEM Discover and held at this temperature for 30 min with continuous stirring. After being cooled to room temperature, the solid was isolated by centrifuging and washed with DMF and acetone.

https://doi.org/10.1021/jacs.1c05032
J. Am. Chem. Soc. 2021, 143, 12220−12229

Synthesis of NiS_{NP}/MOF. Generally, 20 mg of UiO-66-NH_2, 4.7 mg of $NiCl_2 \cdot 6H_2O$, and 50 mg of TAA were dispersed into 3 mL of EtOH, and the mixture was added into a glass reaction tube. The tube was frozen by liquid nitrogen, pumped out air and backfilled protective gas with a N_2 balloon. The reaction tube was heated at the temperature of 85 °C under stirring for 1 h. The resulting black solid was washed with acetone followed by drying under a vacuum at room temperature.

Synthesis of Ni_{NP}/MOF. Generally, 20 mg of Ni^{2+}/MOF was dispersed in 1 mL of methanol. Then, 2 mg of $NaBH_4$ in 1 mL of methanol was introduced into the above solution during vigorous stirring to afford Ni_{NP}/MOF. After stirring for 30 s, the resulting black solid was washed with methanol followed by drying under a vacuum at room temperature.

Synthesis of M_1-S/MOF (M = Co, Cu). The M_1-S/MOF were synthesized by simply replacing the Ni^{2+}/MOF with M^{2+}/MOF (M = Co, Cu), whereas other parameters remain the same.

General Procedure for Photocatalytic H_2 Generation. In a typical experiment, the reaction was performed in a 160 mL photoreactor, purchased from Perfect Light (Beijing, China). The photoreactor was pumped to remove the air and backfilled with 1 atm N_2. The photocatalyst (5 mg unless otherwise stated) was dispersed ultrasonically in a mixture of 4 mL of DMF, 100 μL of deionized water, 1 mL of TEA, and two drops of DMSO, and the suspension was then added into the photoreactor. The photoreactor with reacting solution was irradiated by the Xe lamp (LX-300F, Japan) with the UV cutoff filter (>380 nm). For each evaluation of hydrogen generation, 200 μL of the headspace gas was injected into the GC (Shimadzu GC-2014) and was quantified by a calibration plot to the internal hydrogen standard. The recycling experiment was performed by degassing and backfilling N_2 after every test.

X-ray Absorption Spectroscopy (XAS)..[54−57] The X-ray absorption fine structure (XAFS) spectra (Ni/Co/Cu K-edge) were collected at the 1W1B station in the Beijing Synchrotron Radiation Facility (BSRF). The storage ring of BSRF was operated at 2.5 GeV with an average current of 250 mA. Using an ionization chamber and a Si(111) double-crystal monochromator, the data of Co_1−S/MOF and Cu_1−S/MOF were collected in a fluorescence mode, whereas all the other data were collected in a transmission mode. All spectra were collected under ambient conditions.

Extended X-ray Absorption Fine Structure (EXAFS). The acquired EXAFS data were analyzed by the standard procedures using the ATHENA module implemented in the *IFEFFIT* software packages. The k^3-weighted EXAFS spectra were collected by subtracting the postedge background from the overall absorption and then normalizing with respect to the edge-jump step. Then, k^3-weighted $\chi(k)$ data of Ni K-edge were Fourier transformed to real (R) space using a hanning window (dk = 1.0 $Å^{-1}$) to separate the EXAFS contributions from different coordination shells. To obtain the quantitative structural parameters around central atoms, we carried out least-squares curve parameter fitting using the ARTEMIS module of *IFEFFIT* software packages.

S K-Edge X-ray Absorption near-Edge Structure (XANES). Sulfur K-edge XANES were conducted on the beamline 4B7A at BSRF. Uniform powders of samples and standard materials were pressed into 1 mm-thick slice. The X-ray beam was monochromatized using a fixed-exit double-crystal Si(111) monochromator (0.4 eV resolution). Monochromator energy was calibrated against the peak of the white line of K_2SO_4 at 2482.4 eV. An unfocused beam of about 5 × 3 mm was employed. For samples and standard material powders prepared as thin films on conductive double-sided carbon adhesive tape, we collected XANES spectra in fluorescence yield using a silicon drift diode (e2v, UK) for soil samples and total electron yield mode for the reference materials.

Photoluminescence Emission Spectra. First, 2 mg of catalyst was dispersed ultrasonically in 6 mL of MeCN. The steady-state PL spectra were then measured with a PerkinElmer LS-55 fluorescence spectrometer with the excitation wavelength at 385 nm.

Photocurrent Measurements. Photocurrent measurements were conducted on a CHI 760E electrochemical workstation (Chenhua Instrument, Shanghai, China) in a standard three-electrode system, where the photocatalyst-coated ITO plate as the working electrode, Pt plate as the counter electrode, and Ag/AgCl as a reference electrode. Specifically, 3 mg of catalyst was added into 10 μL of 5 wt % Nafion and 2 mL of ethanol mixed solution, then the working electrodes were prepared by dropping a 300 μL suspension onto the surface of an ITO plate with an area of 4 cm^2. After the working electrodes were dried, the photoresponsive signals of the samples were measured under chopped light at +0.5 V. In this process, a 300 W xenon lamp with full spectrum was used as the light source, and a 0.1 M Na_2SO_4 solution was used as the electrolyte.

Electrochemical Impedance Spectroscopy (EIS). The electrochemical impedance spectroscopy was carried out the Zahner Zennium electrochemical workstation in a standard three-electrode system, with a photocatalyst-coated glassy carbon (Φ = 3 cm) as the working electrode, Pt plate as the counter electrode, and Ag/AgCl as a reference electrode. Specifically, 3 mg of catalyst was added into 10 μL of 5 wt % Nafion and 2 mL of ethanol mixed solution. The working electrode was then prepared by dropping a 30 μL suspension onto the surface of the glassy carbon electrode. After the working electrodes were dried, the EIS measurement was performed with a bias potential of −1.3 V in the dark. In this process, a 0.1 M Na_2SO_4 aqueous solution was used as the electrolyte.

Electron Paramagnetic Resonance (EPR) Spectra. EPR spectra were recorded by JEOL JES-FA200 EPR spectrometer. The solid sample was filled at the bottom of the EPR tube, followed by several freeze−pump−thaw procedures and then backfilling with protective gas (N_2 balloon). The sample was exposed to xenon light irradiation or air atmosphere if necessary. The experiments proceeded at a temperature of 140 K.

Density Functional Theory (DFT) Calculations. All calculations were performed on the VASP 5.4.1.[58] The Projector Augmented Wave (PAW) potentials and Perdew−Burke−Ernzerhof (PBE) functional were adopted to complete the DFT calculations.[59] Moreover, the spin polarization correction and van der Waals correction[60] were included to consider the magnetism effect and weak interaction, respectively. Super large models were built to simulate the Ni_1−S/MOF with 428 atoms, Ni_1−S_{ox}/MOF with 426 atoms, and Ni_1−O/MOF with 427 atoms. Considering the calculation accuracy and cost, a Γ-centered k-point and 450 eV cutoff energy were adopted. The convergence standards of energy and force were selected as 10−5 and 0.05 eV/Å. In addition, the Bader charge was calculated to analyze the charge of Ni atom.[61] The vibrational frequency with finite displacements of ±0.02 Å was performed to obtain the zero-point energy correction and vibrational entropy correction. The Gibbs free energy (G) along the hydrogen reduction reaction pathway was calculated according to the following equation:

$$G = E + \mathrm{ZPE} - T\Delta S \quad (1)$$

Where E is the electronic energy in ground-state obtained from self-consistent calculation, ZPE is the zero-point energy correction obtained from vibrational frequency calculation, T is the temperature (T = 298.15 K), and ΔS is the vibrational entropy correction obtained from the vibrational frequency calculation.

■ ASSOCIATED CONTENT

Supporting Information

The Supporting Information is available free of charge at https://pubs.acs.org/doi/10.1021/jacs.1c05032.

Additional characterizations of metal cation-, single-atom-, and metal nanoparticle-modified MOFs, control experiments, catalytic results, and catalytic mechanism (PDF)

■ AUTHOR INFORMATION

Corresponding Author

Hai-Long Jiang − *Hefei National Laboratory for Physical Sciences at the Microscale, CAS Key Laboratory of Soft*

https://doi.org/10.1021/jacs.1c05032
J. Am. Chem. Soc. 2021, 143, 12220−12229

Matter Chemistry, Department of Chemistry, University of Science and Technology of China, Hefei, Anhui 230026, P. R. China; orcid.org/0000-0002-2975-7977;
Email: jianglab@ustc.edu.cn

Authors

Xing Ma − *Hefei National Laboratory for Physical Sciences at the Microscale, CAS Key Laboratory of Soft Matter Chemistry, Department of Chemistry, University of Science and Technology of China, Hefei, Anhui 230026, P. R. China*

Hang Liu − *Hefei National Laboratory for Physical Sciences at the Microscale, CAS Key Laboratory of Soft Matter Chemistry, Department of Chemistry, University of Science and Technology of China, Hefei, Anhui 230026, P. R. China*

Weijie Yang − *Department of Power Engineering, School of Energy, Power and Mechanical Engineering, North China Electric Power University, Baoding 071003, P. R. China*

Guangyang Mao − *Department of Power Engineering, School of Energy, Power and Mechanical Engineering, North China Electric Power University, Baoding 071003, P. R. China*

Lirong Zheng − *Beijing Synchrotron Radiation Facility, Institute of High Energy Physics, Chinese Academy of Sciences, Beijing 100049, P. R. China*

Complete contact information is available at: https://pubs.acs.org/10.1021/jacs.1c05032

Author Contributions

†X.M. and H.L. contributed equally.

Notes

The authors declare no competing financial interest.

■ ACKNOWLEDGMENTS

This work was supported by the National Natural Science Foundation of China (21725101, 22161142001, and 21521001), the DNL Cooperation Fund, Chinese Academy of Sciences (DNL201911), and the Fundamental Research Funds for the Central Universities (WK3450000007). We thank the 1W1B station for XAFS measurement at the Beijing Synchrotron Radiation Facility (BSRF).

■ REFERENCES

(1) Reece, S. Y.; Hamel, J. A.; Sung, K.; Jarvi, T. D.; Esswein, A. J.; Pijpers, J. J. H.; Nocera, D. G. Wireless solar water splitting using silicon-based semiconductors and earth-abundant catalysts. *Science* **2011**, *334*, 645−648.

(2) Wang, Z.; Li, C.; Domen, K. Recent developments in heterogeneous photocatalysts for solar-driven overall water splitting. *Chem. Soc. Rev.* **2019**, *48*, 2109−2125.

(3) Kim, J. H.; Hansora, D.; Sharma, P.; Jang, J. W.; Lee, J. S. Toward practical solar hydrogen production-an artificial photosynthetic leaf-to-farm challenge. *Chem. Soc. Rev.* **2019**, *48*, 1908−1971.

(4) Wei, L.; Chen, Y.; Lin, Y.; Wu, H.; Yuan, R.; Li, Z. MoS_2 as non-noble-metal co-catalyst for photocatalytic hydrogen evolution over hexagonal $ZnIn_2S_4$ under visible light irradiations. *Appl. Catal., B* **2014**, *144*, 521−527.

(5) Yang, J.; Wang, D.; Han, H.; Li, C. Roles of cocatalysts in photocatalysis and photoelectrocatalysis. *Acc. Chem. Res.* **2013**, *46*, 1900−1909.

(6) Ran, J.; Jaroniec, M.; Qiao, S.-Z. Cocatalysts in semiconductor-based photocatalytic CO_2 reduction: achievements, challenges, and opportunities. *Adv. Mater.* **2018**, *30*, 1704649.

(7) Aiyappa, H. B.; Thote, J.; Shinde, D. B.; Banerjee, R.; Kurungot, S. Cobalt-modified covalent organic framework as a robust water oxidation electrocatalyst. *Chem. Mater.* **2016**, *28*, 4375−4379.

(8) Wang, A.; Li, J.; Zhang, T. Heterogeneous single-atom catalysis. *Nat. Rev. Chem.* **2018**, *2*, 65−81.

(9) Jiao, L.; Jiang, H.-L. Metal-organic-framework-based single-atom catalysts for energy applications. *Chem* **2019**, *5*, 786−804.

(10) Liu, P.; Zhao, Y.; Qin, R.; Mo, S.; Chen, G.; Gu, L.; Chevrier, D. M.; Zhang, P.; Guo, Q.; Zang, D.; Wu, B.; Fu, G.; Zheng, N. Photochemical route for synthesizing atomically dispersed palladium catalysts. *Science* **2016**, *352*, 797−800.

(11) Sun, Q.; Wang, N.; Zhang, T.; Bai, R.; Mayoral, A.; Zhang, P.; Zhang, Q.; Terasaki, O.; Yu, J. Zeolite-encaged single-atom rhodium catalysts: highly-efficient hydrogen generation and shape-selective tandem hydrogenation of nitroarenes. *Angew. Chem., Int. Ed.* **2019**, *58*, 18570−18576.

(12) Ji, S.; Chen, Y.; Wang, X.; Zhang, Z.; Wang, D.; Li, Y. Chemical synthesis of single atomic site catalysts. *Chem. Rev.* **2020**, *120*, 11900−11955.

(13) Liu, J. Catalysis by supported single metal atoms. *ACS Catal.* **2017**, *7*, 34−59.

(14) Zhang, H.; Liu, G.; Shi, L.; Ye, J. Single-atom catalysts: emerging multifunctional materials in heterogeneous catalysis. *Adv. Energy Mater.* **2018**, *8*, 1701343.

(15) Tang, C.; Jiao, Y.; Shi, B.; Liu, J.-N.; Xie, Z.; Chen, X.; Zhang, Q.; Qiao, S.-Z. Coordination tunes selectivity: two-electron oxygen reduction on high-loading molybdenum single-atom catalysts. *Angew. Chem., Int. Ed.* **2020**, *59*, 9171−9176.

(16) Zhao, L.; Zhang, Y.; Huang, L.-B.; Liu, X.-Z.; Zhang, Q.-H.; He, C.; Wu, Z.-Y.; Zhang, L.-J.; Wu, J.; Yang, W.; Gu, L.; Hu, J.-S.; Wan, L.-J. Cascade anchoring strategy for general mass production of high-loading single-atomic metal-nitrogen catalysts. *Nat. Commun.* **2019**, *10*, 1278.

(17) Li, X.; Liu, L.; Ren, X.; Gao, J.; Huang, Y.; Liu, B. Microenvironment modulation of single-atom catalysts and their roles in electrochemical energy conversion. *Sci. Adv.* **2020**, *6*, eabb6833.

(18) Liu, W.; Zhang, L.; Liu, X.; Liu, X.; Yang, X.; Miao, S.; Wang, W.; Wang, A.; Zhang, T. Discriminating catalytically active FeN_x species of atomically dispersed Fe−N−C catalyst for selective oxidation of the C−H bond. *J. Am. Chem. Soc.* **2017**, *139*, 10790−10798.

(19) Chen, Y.; Gao, R.; Ji, S.; Li, H.; Tang, K.; Jiang, P.; Hu, H.; Zhang, Z.; Hao, H.; Qu, Q.; Liang, X.; Chen, W.; Dong, J.; Wang, D.; Li, Y. Atomic-level modulation of electronic density at cobalt single-atom sites derived from metal−organic frameworks: enhanced oxygen reduction performance. *Angew. Chem., Int. Ed.* **2021**, *60*, 3212−3221.

(20) Zhang, B.; Zhang, J.; Shi, J.; Tan, D.; Liu, L.; Zhang, F.; Lu, C.; Su, Z.; Tan, X.; Cheng, X.; Han, B.; Zheng, L.; Zhang, J. Manganese acting as a high-performance heterogeneous electrocatalyst in carbon dioxide reduction. *Nat. Commun.* **2019**, *10*, 2980.

(21) Ren, Y.; Tang, Y.; Zhang, L.; Liu, X.; Li, L.; Miao, S.; Sheng Su, D.; Wang, A.; Li, J.; Zhang, T. Unraveling the coordination structure-performance relationship in Pt_1/Fe_2O_3 single-atom catalyst. *Nat. Commun.* **2019**, *10*, 4500.

(22) Furukawa, H.; Cordova, K. E.; O'Keeffe, M.; Yaghi, O. M. The chemistry and applications of metal-organic frameworks. *Science* **2013**, *341*, 1230444.

(23) Zhou, H.-C.; Kitagawa, S. Metal−organic frameworks (MOFs). *Chem. Soc. Rev.* **2014**, *43*, 5415−5418.

(24) Li, B.; Wen, H.-M.; Cui, Y.; Zhou, W.; Qian, G.; Chen, B. Emerging multifunctional metal−organic framework materials. *Adv. Mater.* **2016**, *28*, 8819−8860.

(25) Wu, G.; Huang, J.; Zang, Y.; He, J.; Xu, G. Porous field-effect transistors based on a semiconductive metal−organic framework. *J. Am. Chem. Soc.* **2017**, *139*, 1360−1363.

(26) Zhai, Q.-G.; Bu, X.; Zhao, X.; Li, D.-S.; Feng, P. Pore space partition in metal−organic frameworks. *Acc. Chem. Res.* **2017**, *50*, 407−417.

(27) Zhang, Y.; Guo, J.; Shi, L.; Zhu, Y.; Hou, K.; Zheng, Y.; Tang, Z. Tunable chiral metal organic frameworks toward visible light−driven asymmetric catalysis. *Sci. Adv.* **2017**, *3*, e1701162.

(28) Li, L.; Wang, X.-S.; Liu, T.-F.; Ye, J. Titanium-based MOF materials: from crystal engineering to photocatalysis. *Small Methods* **2020**, *4*, 2000486.
(29) Wang, S.; Wang, X. Multifunctional metal−organic frameworks for photocatalysis. *Small* **2015**, *11*, 3097−3112.
(30) Huang, Q.; Liu, J.; Feng, L.; Wang, Q.; Guan, W.; Dong, L.-Z.; Zhang, L.; Yan, L.-K.; Lan, Y.-Q.; Zhou, H.-C. Multielectron transportation of polyoxometalate−grafted metalloporphyrin coordination frameworks for selective CO_2−to−CH_4 photoconversion. *Natl. Sci. Rev.* **2020**, *7*, 53−63.
(31) Pattengale, B.; Yang, S.; Ludwig, J.; Huang, Z.; Zhang, X.; Huang, J. Exceptionally long-lived charge separated state in zeolitic imidazolate framework: implication for photocatalytic applications. *J. Am. Chem. Soc.* **2016**, *138*, 8072−8075.
(32) Zhang, H.; Wei, J.; Dong, J.; Liu, G.; Shi, L.; An, P.; Zhao, G.; Kong, J.; Wang, X.; Meng, X.; Zhang, J.; Ye, J. Efficient visible-light-driven carbon dioxide reduction by a single-atom implanted metal−organic framework. *Angew. Chem., Int. Ed.* **2016**, *55*, 14310−14314.
(33) Jiao, L.; Wang, J.; Jiang, H.-L. Microenvironment Modulation in Metal-Organic Framework-Based Catalysis. *Acc. Mater. Res.* **2021**, *2*, 327−339.
(34) Xu, C.; Pan, Y.; Wan, G.; Liu, H.; Wang, L.; Zhou, H.; Yu, S.-H.; Jiang, H.-L. Turning on visible-light photocatalytic C−H oxidation over metal−organic frameworks by introducing metal-to-cluster charge transfer. *J. Am. Chem. Soc.* **2019**, *141*, 19110−19117.
(35) Abdel-Mageed, A. M.; Rungtaweevoranit, B.; Parlinska-Wojtan, M.; Pei, X.; Yaghi, O. M.; Behm, R. J. Highly active and stable single-atom Cu catalysts supported by a metal−organic framework. *J. Am. Chem. Soc.* **2019**, *141*, 5201−5210.
(36) Fang, X.; Shang, Q.; Wang, Y.; Jiao, L.; Yao, T.; Li, Y.; Zhang, Q.; Luo, Y.; Jiang, H.-L. Single Pt atoms confined into a metal-organic framework for efficient photocatalysis. *Adv. Mater.* **2018**, *30*, 1705112.
(37) Pi, Y.; Feng, X.; Song, Y.; Xu, Z.; Li, Z.; Lin, W. Metal−organic frameworks integrate Cu photosensitizers and secondary building unit-supported Fe catalysts for photocatalytic hydrogen evolution. *J. Am. Chem. Soc.* **2020**, *142*, 10302−10307.
(38) Islamoglu, T.; Goswami, S.; Li, Z.; Howarth, A. J.; Farha, O. K.; Hupp, J. T. Postsynthetic tuning of metal−organic frameworks for targeted applications. *Acc. Chem. Res.* **2017**, *50*, 805−813.
(39) Planas, N.; Mondloch, J. E.; Tussupbayev, S.; Borycz, J.; Gagliardi, L.; Hupp, J. T.; Farha, O. K.; Cramer, C. J. Defining the proton topology of the Zr_6-based metal-organic framework NU-1000. *J. Phys. Chem. Lett.* **2014**, *5*, 3716−3723.
(40) Yang, H. B.; Hung, S.-F.; Liu, S.; Yuan, K.; Miao, S.; Zhang, L.; Huang, X.; Wang, H.-Y.; Cai, W.; Chen, R.; Gao, J.; Yang, X.; Chen, W.; Huang, Y.; Chen, H. M.; Li, C. M.; Zhang, T.; Liu, B. Atomically dispersed Ni(I) as the active site for electrochemical CO_2 reduction. *Nat. Energy* **2018**, *3*, 140−147.
(41) Peters, A. W.; Li, Z.; Farha, O. K.; Hupp, J. T. Toward inexpensive photocatalytic hydrogen evolution: a nickel sulfide catalyst supported on a high-stability metal−organic framework. *ACS Appl. Mater. Interfaces* **2016**, *8*, 20675−20681.
(42) Nesbitt, H. W.; Legrand, D.; Bancroft, G. M. Interpretation of Ni2p XPS spectra of Ni conductors and Ni insulators. *Phys. Chem. Miner.* **2000**, *27*, 357−366.
(43) Huang, L.; Wang, G.; Qin, Z.; Du, M.; Dong, M.; Ge, H.; Wu, Z.; Zhao, Y.; Ma, C.; Hu, T.; Wang, J. A sulfur K-edge XANES study on the transfer of sulfur species in the reactive adsorption desulfurization of diesel oil over Ni/ZnO. *Catal. Commun.* **2010**, *11*, 592−596.
(44) Muryn, C. A.; Purdie, D.; Hardman, P.; Johnson, A. L.; Prakash, N. S.; Raiker, G. N.; Thornton, G.; Law, D. S-L. Sulphur-induced structural chemistry of oxide surfaces. *Faraday Discuss. Chem. Soc.* **1990**, *89*, 77−89.
(45) Fang, Z.-B.; Liu, T.-T.; Liu, J.; Jin, S.; Wu, X.-P.; Gong, X.-Q.; Wang, K.; Yin, Q.; Liu, T.-F.; Cao, R.; Zhou, H.-C. Boosting interfacial charge-transfer kinetics for efficient overall CO_2 photoreduction via rational design of coordination spheres on metal−organic frameworks. *J. Am. Chem. Soc.* **2020**, *142*, 12515−12523.
(46) Rabo, J. A.; Angell, C. L.; Kasai, P. H.; Schomaker, V. Studies of cations in zeolites: adsorption of carbon monoxide; formation of Ni ions and Na^{3+}_4 centres. *Discuss. Faraday Soc.* **1966**, *41*, 328−349.
(47) Derouane, E. G.; Braham, J. N.; Hubin, R. EPR study of the oxidative coupling reaction of aniline homogeneously catalyzed by $Cu(C_5H_5N)_4(NO_3)_2$. *J. Catal.* **1974**, *35*, 196−201.
(48) Janovský, I.; Knolle, W.; Naumov, S.; Williams, F. EPR studies of amine radical cations, part 1: thermal and photoinduced rearrangements of *n*-alkylamine radical cations to their distonic forms in low-temperature freon matrices. *Chem. - Eur. J.* **2004**, *10*, 5524−5534.
(49) Schaate, A.; Roy, P.; Godt, A.; Lippke, J.; Waltz, F.; Wiebcke, M.; Behrens, P. Modulated synthesis of Zr-based metal−organic frameworks: from nano to single crystals. *Chem. - Eur. J.* **2011**, *17*, 6643−6651.
(50) Shearer, G. C.; Chavan, S.; Bordiga, S.; Svelle, S.; Olsbye, U.; Lillerud, K. P. Defect engineering: tuning the porosity and composition of the metal−organic framework UiO-66 via modulated synthesis. *Chem. Mater.* **2016**, *28*, 3749−3761.
(51) Ma, X.; Wang, L.; Zhang, Q.; Jiang, H.-L. Switching on the photocatalysis of metal−organic frameworks by engineering structural defects. *Angew. Chem., Int. Ed.* **2019**, *58*, 12175−12179.
(52) Furukawa, H.; Gándara, F.; Zhang, Y.-B.; Jiang, J.; Queen, W. L.; Hudson, M. R.; Yaghi, O. M. Water adsorption in porous metal−organic frameworks and related materials. *J. Am. Chem. Soc.* **2014**, *136*, 4369−4381.
(53) Reinsch, H.; Waitschat, S.; Chavan, S. M.; Lillerud, K. P.; Stock, N. A facile "Green" route for scalable batch production and continuous synthesis of zirconium MOFs. *Eur. J. Inorg. Chem.* **2016**, *27*, 4490−4498.
(54) Ravel, B.; Newville, M. *ATHENA, ARTEMIS, HEPHAESTUS*: data analysis for X-ray absorption spectroscopy using IFEFFIT. *J. Synchrotron Radiat.* **2005**, *12*, 537−541.
(55) Koningsberger, D. C.; Prins, R. *X-ray Absorption: Principles, Applications, Techniques of EXAFS, SEXAFS, and XANES*; Chemical Analysis 92; Wiley, 1988.
(56) Rehr, J. J.; Albers, R. C. Theoretical approaches to x-ray absorption fine structure. *Rev. Mod. Phys.* **2000**, *72*, 621−654.
(57) Zheng, L.; Zhao, Y. D.; Tang, K.; Ma, C. Y.; Hong, C. H.; Han, Y.; Cui, M. Q.; Guo, Z. Y. A new experiment station on beamline 4B7A at Beijing Synchrotron Radiation Facility. *Spectrochim. Acta, Part B* **2014**, *101*, 1−5.
(58) Kresse, G.; Furthmüller, J. Efficient iterative schemes for *ab initio* total-energy calculations using a plane-wave basis set. *Phys. Rev. B: Condens. Matter Mater. Phys.* **1996**, *54*, 11169−11186.
(59) Perdew, J. P.; Burke, K.; Ernzerhof, M. Generalized gradient approximation made simple. *Phys. Rev. Lett.* **1996**, *77*, 3865−3868.
(60) Grimme, S.; Antony, J.; Ehrlich, S.; Krieg, H. A consistent and accurate *ab initio* parametrization of density functional dispersion correction (DFT-D) for the 94 elements H-Pu. *J. Chem. Phys.* **2010**, *132*, 154104.
(61) Tang, W.; Sanville, E.; Henkelman, G. A grid-based Bader analysis algorithm without lattice bias. *J. Phys.: Condens. Matter* **2009**, *21*, 084204.

https://doi.org/10.1021/jacs.1c05032
J. Am. Chem. Soc. 2021, 143, 12220−12229